



High-throughput microfluidics for evaluating microbubble enhanced delivery of cancer therapeutics in spheroid cultures



Matthew D. Bourn^{a,b}, Damien V.B. Batchelor^a, Nicola Ingram^b, James R. McLaughlan^{b,c}, P. Louise Coletta^b, Stephen D. Evans^a, Sally A. Peyman^{a,b,*}

^a School of Physics and Astronomy, University of Leeds, Leeds LS2 9JT, United Kingdom

^b Leeds Institute for Medical Research, Wellcome Trust Brenner Building, St James' University Hospital, Leeds LS9 7TF, United Kingdom

^c School of Electronic and Electrical Engineering, University of Leeds, LS2 9JT, United Kingdom

ARTICLE INFO

Keywords:

Drug delivery
Tumour-on-chip
Microbubbles
Ultrasound
Microfluidics
Spheroid trap

ABSTRACT

Drug penetration into solid tumours remains a major challenge in the effective treatment of cancer. Microbubble (MB) mediated sonoporation offers a potential solution to this by enhancing the uptake of drugs into cells. Additionally, in using an ultrasound (US) trigger, drug delivery can be localised to the tumour, thus reducing the off-site toxicity associated with systemic delivery. The majority of *in vitro* studies involving the observation of MB-enhanced drug efficacy have been conducted on 2D monolayer cell cultures, which are known to be poor models for *in vivo* tumours. 3D spheroid cultures allow for the production of multicellular cultures complete with extracellular matrix (ECM) components. These cultures effectively recreate many of the physiological features of the tumour microenvironment and have been shown to be far superior to previous 2D monolayer models. However, spheroids are typically handled in well-plates in which the fluid environment is static, limiting the physiological relevance of the model. The combination of 3D cultures and microfluidics would allow for the production of a dynamic system in which spheroids are subjected to *in vivo* like fluid flow and shear stresses. This study presents a microfluidic device containing an array of spheroid traps, into which multiple pre-grown colorectal cancer (CRC) spheroids were loaded. Reservoirs interfaced with the chip use hydrostatic pressure to passively drive flow through the system and subject spheroids to capillary like flow velocities. The use of reservoirs also enabled multiple chips to be run in parallel, allowing for the screening of multiple therapeutic treatments ($n = 690$ total spheroids analysed). This microfluidic platform was used to investigate MB enhanced drug delivery and showed that co-delivery of $3 \mu\text{M}$ doxorubicin (DOX) + MB + US reduced spheroid viability to $48 \pm 2\%$, compared to $75 \pm 5\%$ observed with $3 \mu\text{M}$ DOX alone. Delivery of drug loaded MBs (DLMBs), in which DOX-loaded liposomes (DOX-LS) were conjugated to MBs, reduced spheroid viability to $62 \pm 3\%$, a decrease compared to the $75 \pm 3\%$ viability observed with DOX-LS in the absence of MBs + US.

1. Introduction

Typical *in vitro* 2D monolayer cell cultures used to test many potential anticancer therapeutics fail to effectively recreate many physiological features of *in vivo* tumours [1]. While they present valuable simplistic models to investigate fundamental biology, their use as drug assessment platforms are limited. Drugs that appear to have high efficacy against monolayer models, often don't translate these outcomes to more complex *in vivo* systems. Monolayer cultures lack cell-cell connections, multicellular compositions and extracellular matrix (ECM) components, resulting in their failure to produce results observed in the clinic [1–3]. 3D spheroid culture models have been developed to help

overcome many of these shortcomings, using aggregates of multiple cell types to form 3D tumour cultures. Moreover, the structure of solid tumours is more faithfully recreated in spheroids, which consist of a necrotic core with a surrounding hypoxic region composed of quiescent cells bounded by a rapidly proliferating outer layer [4,5]. Indeed, it has been shown that the 3D tumour co-cultures produce a model which more effectively predicts the clinical effects of anticancer drugs, compared to 2D model counterparts [2,6–8].

The inclusion of fibroblasts into 3D spheroid cultures has proved to be a crucial component in creating a physiological tumour model. Fibroblasts cultured alongside tumour cells differentiate to become cancer-associated fibroblasts (CAFs), also known as myofibroblasts

* Corresponding author at: School of Physics and Astronomy, University of Leeds, Leeds LS2 9JT, United Kingdom.

E-mail address: s.peyman@leeds.ac.uk (S.A. Peyman).

<https://doi.org/10.1016/j.jconrel.2020.06.011>

Received 5 March 2020; Received in revised form 12 May 2020; Accepted 11 June 2020

Available online 17 June 2020

0168-3659/ Crown Copyright © 2020 Published by Elsevier B.V. This is an open access article under the CC BY license (<http://creativecommons.org/licenses/by/4.0/>).

[9–11]. Characterised by the expression of alpha smooth muscle actin (α -SMA), CAFs secrete a myriad of growth factors, chemokines and ECM proteins that promote tumour growth, metastasis and drug resistance [11–16]. Responsible for many of the physical characteristics tumours display, CAFs increase the stiffness and density of the tumour ECM, limiting the penetration and effectiveness of many chemotherapeutics. Several studies have investigated the link between the presence of CAFs and the progression of colorectal cancers (CRCs), finding that an abundance of CAFs is associated with more aggressive tumours and a lower overall rate of disease free survival [12,17–20]. This emphasises the need for the incorporation of multiple cell types in tumour cultures, if a physiologically relevant model is to be achieved to improve the accuracy in predicting drug efficacy in pre-clinical testing.

The rise of spheroid cultures for drug toxicity assays has highlighted one of the main issues with current cancer treatment methods – the lack of drug penetration into solid tumours. The physical barrier of ECM proteins produced by CAFs, along with inherent drug resistance displayed by quiescent cells, results in many anticancer drugs failing to have a significant effect on tumour progression [11,21–23]. MB-mediated sonoporation, induced by the application of an ultrasound (US) wave, offers a promising solution to this issue and has been studied extensively as a method by which drug uptake in cells can be increased [24–31]. US alone has been shown to increase membrane permeability through the formation of membrane pores [32,33]. This effect is increased in the presence of MBs, which undergo oscillations that can result in jet formation and localised shear flow, disrupting nearby cell membranes [34,35]. This has been shown to effectively deliver target molecules to cells, specifically enhancing drug uptake due to the openings created in cell membranes. The majority of these studies, however, have been conducted on 2D monolayers of cells, meaning MB effectiveness in 3D cultures is still relatively undocumented. Recent studies have begun testing MB therapies on 3D static spheroid cultures, observing the effects of delivering drug-loaded liposomes conjugated to MBs. Roovers et al. have shown that MB-induced sonoporation results in the ‘sonoprinting’ of liposomes (LSs) from DOX-LS-loaded MBs onto the spheroid surface. This resulted in increased liposome cytotoxicity compared to LSs alone and was hypothesised to allow for lower doses of DOX to be administered in the clinic with the same efficacy [36]. Logan et al. observed similar effects and also incorporated drugs sensitive to US-induced cavitation into the MB complex [37].

Previous MB-spheroid studies have neglected to incorporate any fluid flow conditions into their systems, a physical parameter that is vastly important in tissues and drug delivery. The lack of fluid flow fails to recreate the constant supply and removal of nutrients and waste products experienced *in vivo*, as well as failing to subject cells to appropriate shear stresses. In addition, most therapeutic agents are delivered by direct injection into the cardiovascular system, and interact with tissues under flow conditions. Microfluidic technology offers a solution to these limitations, allowing for the maintenance of spheroid cultures under constant flow. As a result, various microfluidic spheroid culture systems have been developed, using micro-well arrays, trapping chambers and droplet-based microfluidics to culture and trap spheroids [38–43]. Previous trapping chambers have employed the use of gravity traps to capture pre-grown spheroids. This method allows for a high trapping efficiency, but it is relatively low throughput. In addition, the spheroids cannot be recovered from the traps, therefore analysis is limited to imaging-based assays only. Single-cell suspensions are often seeded into microfluidic spheroid systems to allow for on-chip formation of spheroids. Whilst this has the advantage of forming high numbers of spheroids under flow, the narrow cell loading channels often do not allow for retrieval of the spheroids after treatment, again meaning quantitative assays cannot be performed. Qualitative data obtained from imaging of spheroids using fluorescence microscopy alone can also be problematic to quantify, due to the scattering effects observed towards the centre of large spheroids.

We present a microfluidic system that allows for high numbers of

spheroids to be exposed to therapeutic agents under physiologically relevant flow conditions. Spheroids were trapped in microfluidic devices and subjected to passive, gravity driven flow with velocities mimicking those found in blood capillaries (0.3–1 mm/s) [44]. The use of integrated reservoirs over conventional syringe pumps eliminated the issues associated with operating syringe pumps and tubing in conjunction with an incubator. Furthermore, separate media sources allowed multiple devices to be ran in parallel with different therapeutic exposures. Each experiment allowed for up to 100 spheroids to be trapped across 12 self-contained devices, each of which could be subjected to a variety of therapeutic exposures. The trap design also allowed for simple spheroid retrieval by the reversal of flow, enabling the quantitative analysis of spheroid viability off-chip using an Adenosine TriPhosphate (ATP) viability assay. Overall, this system provided a platform which could supply physiological rates of fluid flow to pre-grown HCT116 colorectal cancer (CRC) and Human Foetal Foreskin Fibroblast (HFFF2) spheroids. Spheroid cultures could be easily trapped, exposed to therapeutics under flow, and retrieved for quantitative analysis. This system was subsequently used to investigate the effect of MB-enhanced drug delivery on spheroid viability. The effect of free and liposomal doxorubicin (DOX) co-delivered with US activated MBs was investigated and compared to the effects of DOX alone. Confocal imaging and ATP assay results showed that MBs enhanced both drug accumulation and efficacy in both free and liposomal treatments.

2. Materials and methods

2.1. Cell culture and spheroid production

HCT116 (ECACC 91091005) and HFFF2 (ECACC 86031405) were both originally obtained from ECACC (UK). Cells were STR profiled to ensure authenticity and regularly tested for mycoplasma. Cells were grown and maintained in DMEM 10% FBS (Thermo Fisher, UK), with 1% Glutamax (Gibco, UK), in an incubator at 37 °C, 5 % CO₂. 200 μ L of a 7.5×10^2 cells/mL cell suspension in a 1:1 HCT116 - HFFF2 ratio was seeded into ultra-low attachment 96 well-plates (Corning, Costar) and spheroids were allowed to develop for 5 days.

2.2. Microfluidic device fabrication

Polydimethylsiloxane (PDMS) microfluidic devices were fabricated using standard photolithography and soft lithography techniques [45,46]. SU8-2075 photoresist was spin coated onto a 3-in. silicon wafer then baked for 90 min. This process was repeated, giving a total resist height of approximately 350 μ m. A direct write 375 nm UV laser (DWL, Durham Magneto Optics) selectively exposed the photoresist and patterned the microfluidic design. The wafer was baked for a further 90 min then excess photoresist removed using Microposit EC solvent (Dow, US). PDMS (Sylgard 184, Dowsil) was mixed in a 10:1 base:curing agent ratio, poured onto the wafer and desiccated for 40 min to remove any bubbles. PDMS was then cured at 80 °C for a 1 h. Devices were then cut, hole-punched and bonded to PDMS coated glass microscope slides using oxygen plasma. Fabricated devices were then sterilised in an autoclave at 120°C for 40 min. Reservoirs were fabricated from 16 mm diameter polycarbonate (Engineering & Design Plastics) cut into 32 mm long pieces. Reservoirs were fabricated to contain a 2 mm wide spout protruding from the bottom of each container. This allowed for simple interfacing with 2 mm hole-punched inlets and outlets in the microfluidic. Lids were fabricated by gluing 0.22 μ m PTFE filters (Cole-Parmer) onto the top of Delrin (Par-group) rings, which then slotted over the top of the reservoirs. 0.22 μ m filters prevented bacterial contamination of the media. Reservoirs were autoclaved at 120°C for 40 min and the underside of the reservoir lids sterilised under UV light for 30 min prior to experimental use.

2.3. Device setup and operation

As a first step, each device was flushed with ethanol to wet the channel surfaces and ensure no air bubbles remained lodged within the traps. The inlet and outlet of each device could be accessed directly through the bottom of each reservoir using a 200 μL pipette. Ethanol was removed and the device flushed through with PBS (+Ca, +Mg, Gibco, UK) then DMEM 10% FBS (Thermo Fisher, UK), 1% Glutamax (Gibco, UK). Spheroids were then collected from each low-adhesion well and deposited into the inlet reservoir. Prior to loading, spheroids were imaged and sized using SpheroidSizer [47]. Spheroids with a diameter in the range of 280–350 μm were then identified for loading on chip. 10 spheroids were loaded into each inlet reservoir and allowed to flow into the device. The hydrodynamic force from media flow ensured that spheroids remained in their traps, unless subjected to backflow. Once spheroids had been trapped, media from both reservoirs was removed and the therapeutic compound added to the inlet reservoir. For MB exposures, MBs were directly pipetted into the channel through the reservoir spout, preventing MBs from rising to the top of the reservoir by their intrinsic buoyancy. The MB sample was pipetted up to the end of the inlet serpentine channel, meaning no MBs passed through the chamber at high rates of flow. Excess sample was deposited into the reservoir before media was added to induce flow at the desired flow rates. Therapeutic exposure was stopped by simply removing all compound-containing media and refilling the inlet reservoir with fresh media.

2.4. DOX preparation and DOX-LS production

DOX (100 mg, Generon, UK) was dissolved in 5 mL DMSO then further diluted in DMEM to the required concentration (1–10 μM). DMSO concentration was kept below 0.5% (v/v) to limit toxicity and prevent any reduction in cell viability. LS (55mol % DSPC, 40mol % Cholesterol and 5mol % DSPE-PEG2000 (Lipoid, GE)) were produced via extrusion through a 200 nm filter membrane. LS were extruded in ammonium sulphate (300 mM), with the pH adjusted to 7.2 using sodium hydroxide (0.1 M). LS were then dialysed in sterile ultrapure water overnight to remove any excess buffer. DOX hydrochloride (4 mg/mL, Fluorochem, UK) was then loaded into the LS, using the pH gradient from the ammonium salt to actively load the DOX. Unencapsulated DOX was removed using a NAP-5 gel filtration column (GE Healthcare, USA). LS concentration was determined using a NanoSight NS300 (Malvern Panalytical) and typically found to be $2\text{--}4 \times 10^{12}$ LS/mL. The amount of DOX encapsulated inside the LS was determined by comparing absorbance at 500 nm of a known, lysed concentration of LS with a DOX calibration curve produced using the absorbance of known DOX concentrations. LS were lysed using 0.2% Triton X-100 (Sigma, UK) and the absorbance measured using a UV-Vis-NIR spectrophotometer (Cary 5000, Agilent, USA). 1×10^{10} LS were found to contain, on average, 3.5 μg of DOX. This gave an approximate encapsulation efficiency of 79% after cleaning.

2.5. MB and DLMB production

MBs were prepared from a mixture of DPPC and DSPE-PEG2000 in a 95:5 M ratio and a total lipid concentration of 2 mg/mL. Lipids were dissolved in a 1:1 mixture of chloroform and methanol and dried under nitrogen to remove the solvent, then resuspended in PBS solution containing 1% glycerol in a sonicating water bath. The lipid solution was then combined with C_4F_{10} gas in a microfluidic device for MB production as described previously [48]. After production, the MB size and concentration distribution were measured optically using bright-field microscopy and analysed using a custom MATLAB (2017b, MathWorks, USA) script. MBs were diluted in PBS to a final concentration of $\sim 10^8$ MB/mL with an average diameter between 1 and 2 μm (Supplementary Fig. S1). Experiments containing fluorescent MBs

used DOPE Atto488 lipids (0.2%) in MB production. DLMBs were produced using 5% DSPE-PEG2000-Biotin (Avanti Polar Lipids, USA) in both MB and LS preparations. Neutravidin (10 μM , ThermoFisher Scientific, USA) was then used to bind LS and MBs.

2.6. Ultrasound instrumentation and exposure

Microfluidic devices were insonated using a 2.25 MHz centre frequency unfocused transducer (V323-SM, Olympus, US). Ultrasound pulses were controlled by a function generator (TG5011, Agilent Technologies, UK) and consisted of a duty cycle of 1%, pulse repetition frequency of 1 kHz for a total duration of 2 s. The free field transducer output was calibrated using a 0.2 mm needle hydrophone (Precision Acoustics, UK) to provide a peak negative pressure of 0.81 ± 0.04 MPa when driven by a + 53 dB RF power amplifier (A150, Electronics % Innovation, US). The transducer was coupled to the top of the microfluidic device via a gel pad (Aquaflex, Parker Laboratories, US) and coupling gel. Use of a gel standoff pad meant that the spheroid chamber was further than the Rayleigh distance away from the transducer, ensuring that the spheroid chamber was exposed to the far field, uniform US beam. The PDMS device was fabricated to be 1 mm thick to minimise US attenuation. Peak negative pressure with 1 mm of PDMS in front of the hydrophone was measured to be 0.81 ± 0.04 MPa, a reduction from 0.94 ± 0.01 MPa in degassed ultrapure water. This gave a Mechanical Index (MI) of 0.54 ± 0.03 . The pressures recorded with the hydrophone only gave an approximation for the acoustic pressure produced on-chip, as attenuation due to PDMS alone is an oversimplification. Local pressure variations will arise due to acoustic reflections from the glass coverslip and device geometry. Nevertheless, complete acoustic characterisation of the system was not necessary, as total destruction of the MBs was the only requirement for this investigation.

2.7. ATP viability assay

CellTiter-Glo 3D cell viability assay (Promega, USA) was used as an endpoint assay to determine spheroid viability. Spheroids were retrieved from the chip 48 h after exposure by withdrawing via a pipette inserted into the inlet reservoir. The lack of adhesion between cells and PDMS means spheroids can be easily dislodged by backflow. Spheroids were allowed to grow a further 48 h after exposure to allow for measurement of the chemotherapeutic effect on cell division. Untreated control spheroids were grown for the same length of time and used in comparison. Spheroids from each chip were deposited in a volume of 100 μL into each well of an opaque-walled 96 well-plate. 100 μL of assay reagent was mixed into each well and incubated at room temperature for 30 min. Luminescence was then recorded on a plate reader (SpectraMax M2E, Molecular Devices, USA) as per assay instructions. To account for variation in initial spheroid diameter, and by extension volume, final luminescence values were normalised with respect to a 300 μm diameter spheroid. Normalisation factors were determined for each chip using the average volume of the 10 spheroids loaded.

2.8. Confocal imaging

A Leica DMi8/SP8 confocal microscope system was used for fluorescence imaging of spheroids. DOX and NucRed Dead dye (Thermo Fisher Scientific, USA) were excited sequentially using 488 nm OPSP and 638 nm Diode lasers respectively. Fluorescence emission for DOX was measured from 410 to 493 nm and for NucRed Dead emission between 651 and 799 nm. Images were acquired approximately 100 μm from the top of the chamber, allowing the upper sections of the spheroid to be viewed. A 10 \times objective was used with the confocal pinhole set to 2 A.U., giving an approximate axial image thickness of 19 μm .

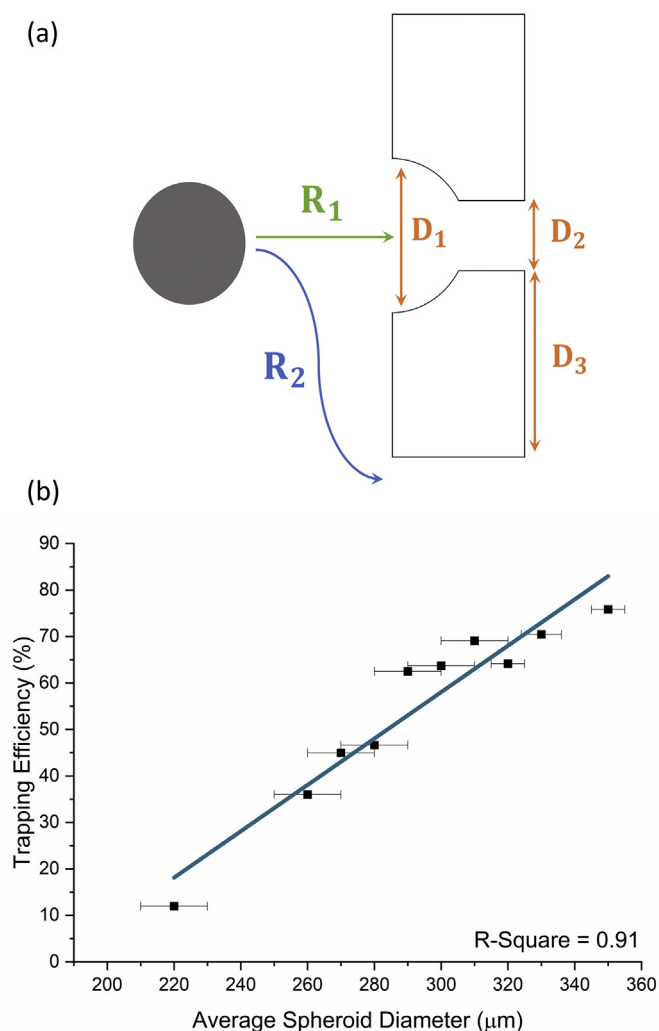


Fig. 1. a) Diagram showing spheroid trap dimensions and the hydraulic resistance for fluid flowing through, R_1 or around, R_2 the trap. b) Plot of observed trapping efficiency against average spheroid diameter. Average of 56 spheroids per point.

3. Results and discussion

3.1. Device design and optimisation

In order to capture as many spheroids as possible and improve assay statistics, careful consideration of the design of the microfluidic device was required. Fig. 1a shows a single spheroid trap with dimensions (orange D_1 , D_2 and D_3) and fluidic resistances associated with flow through and around the obstacle (green R_1 and blue R_2 lines). The spheroid traps were designed by considering the ratio of hydraulic resistances through, R_1 , and around, R_2 , each trap. These hydraulic resistances are dependent on trap dimensions such as trap diameter, D_1 (300–350 μm), centre channel width, D_2 (120–250 μm), trap length, D_3 (400–600 μm), and distance between traps (400 μm). These calculations were originally considered by Xu et al. (2013), who used this technique to optimise the trapping of 5 μm microspheres in trap arrays [49]. The same framework was applied to this scaled-up system to optimise trap geometry for the trapping of 320 μm spheroids. The overall trap array design was based on single-cell culture arrays originally designed by Di Carlo et al. [50]. The main development from this initial design is the inclusion of a central trap channel, the primary function of which is to control resistances through the array.

Resistances through and around each trap were calculated to be on

the order of 10^{-9} Pa. s/ m^3 . Traps with resistance ratios (R_1/R_2) from 1 to 5 were designed and modelled in Ansys Fluent (Supplementary Fig. S2) to observe the change in flow behaviour through each trap. Traps were then fabricated and tested to determine the trapping efficiency, defined as the total number of spheroids trapped out of the 10 loaded onto each chip. A resistance ratio of 2.1 was determined to be optimal for this system, resulting in a trapping efficiency, on average, of 70 % for 320 μm spheroids. Traps with a lower ratio, such as 1.3, were created by widening the centre channel to 250 μm . This however, resulted in spheroids deforming through the centre of the traps when under high flow rates (≥ 0.8 $\mu\text{L/s}$). Higher ratios of ≥ 3.1 reduced the flow through each trap in turn, reducing the probability of a spheroid becoming trapped. The ratio chosen balanced each of these effects to optimise trapping efficiency. In addition to the resistance ratio, trapping efficiency was also found to be dependent on spheroid diameter. Fig. 1b shows a plot of trapping efficiency (%) against average spheroid diameter (μm) for traps with a resistance ratio of 2.1, recorded over several experiments. As the spheroid size increased from 220 μm to 350 μm in diameter, the trapping efficiency also increased from $\sim 10\%$ to 75%. Again, high flow rates (≥ 0.8 $\mu\text{L/s}$) used in spheroid loading caused smaller spheroids (< 280 μm) to overshoot the traps or deform through the centre channel, decreasing the trapping efficiency. A mean occupancy of 6 ± 2 spheroids per chip was achieved across all experiments (minimum of 1, maximum of 11). Together, this consistent trapping efficiency and chip parallelisation allowed for high throughput spheroid testing compared to pre-existing microfluidic spheroid systems.

Fig. 2a shows a schematic of the microfluidic trap system, showing the centre array containing 17 individual traps used to capture the spheroids and long serpentine channels to increase device hydraulic resistance and regulate flow rate. Fig. 2b shows a brightfield microscopy image of spheroids trapped inside the chamber of the device. As an alternative to using conventional syringe pumps, fluid was driven passively through the device using integrated reservoirs and hydrostatic pressure. This allowed for multiple systems to be run in parallel without the need for large numbers of syringe pumps, enabling the high throughput testing of multiple therapeutics. Reservoirs were slotted into the inlet and outlet of each device, then the inlet reservoir filled with media to initiate flow (Supplementary Fig. S3). The height difference in fluid levels in inlet and outlet reservoirs results in a hydrostatic pressure imbalance, inducing fluid flow until levels have equilibrated. Flow rates through the device were then dependent on the difference between inlet and outlet reservoir fluid levels, as well as the channel geometry.

Serpentine channels, each 13 mm long, were used to increase the hydraulic resistance of the device and reduce the flow rate to produce capillary-like flow in the spheroid chamber. Fig. 2c shows a plot of theoretical flow rate and measured flow rate, determined by tracking the trajectory of 2 μm fluorescent beads. Beads were recorded flowing through the chamber and their linear velocities were determined using MosaicSuite ImageJ particle tracking plugin (<http://mosaic.mpi-cbg.de/?q=downloads/imageJ>). Linear velocities were found to vary between 0.2 and 0.85 mm/s through the chamber for reservoir height differences of 5–20 mm, corresponding to volumetric flow rates of 0.19–0.78 $\mu\text{L/s}$. From these observations, the hydraulic resistance throughout the entire system was determined to be $(2.5 \pm 0.1) \times 10^{11}$ Pa. s/ m^3 . This was lower than the theoretical resistance of 3.6×10^{11} Pa. s/ m^3 calculated using the Poiseuille flow solution for rectangular shaped channels [51]. This disagreement can, in part, be attributed to an assumption made in the Poiseuille flow model when calculating the hydraulic resistance of the channel. This assumes a very flat, wide channel ($h/w \rightarrow 0$) which was not the case for the serpentine channels in this device ($h/w \approx 1$) [51]. Nevertheless, flow rates achieved through the use of reservoirs successfully emulated flow velocities found within capillaries (0.3–1 mm/s). The resulting shear stress induced from these flow rates was estimated by modelling flow passing

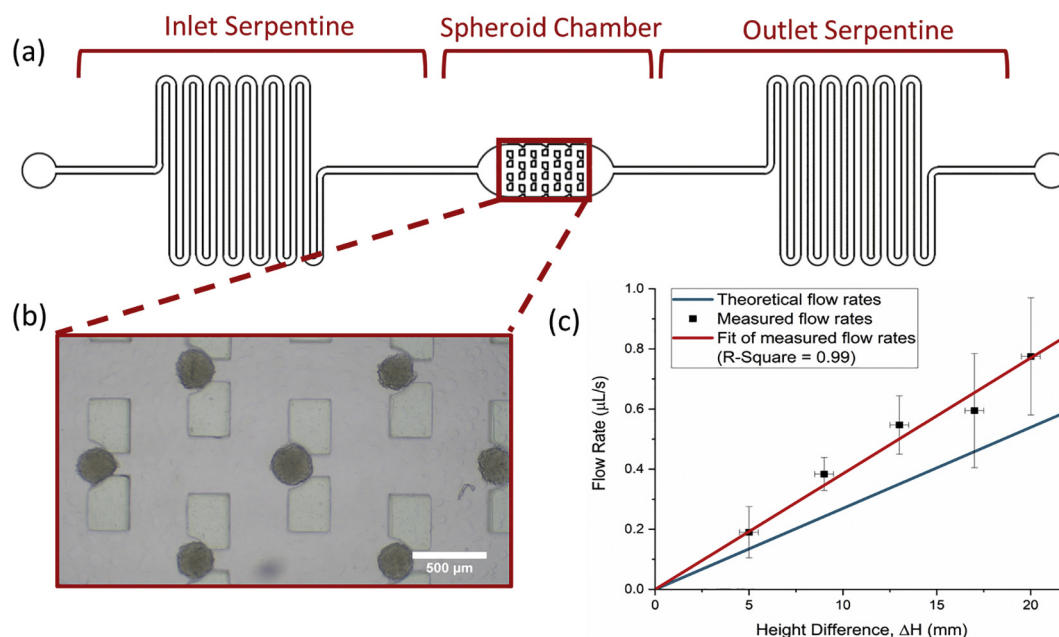


Fig. 2. a) Spheroid trap design showing serpentine channels and a central trapping chamber. b) Multiple HCT116 – HFFF2 spheroids trapped within the trap array. c) Plot of theoretical and measured flow rates against the difference in the inlet and outlet reservoir fluid heights.

over spheroids occupying the traps (Supplementary Fig. 4). It was found that the average shear stress experienced by each spheroid was 11 ± 2 dynes/cm², well within the physiological range of 1–70 dynes/cm² [52].

3.2. Spheroid response to free doxorubicin

To demonstrate the suitability of the microfluidic device for high-throughput screening, a proof-of-principle exposure of trapped spheroids to free DOX was performed. This experiment also allowed for the 50% inhibitory concentration (IC₅₀) to be determined for spheroids on-chip. Off-chip exposure of DOX to monoculture and co-culture spheroids revealed that DOX concentrations between 0 and 10 μM resulted in a typical dose response curve (Supplementary Fig. S5). IC₅₀ values were determined to be 0.9 ± 0.1 μM and 1.9 ± 0.2 μM for monoculture and co-culture spheroids, respectively. This range was therefore used to determine the on-chip dose-response. The exposure of spheroids to free DOX and the corresponding change in cell viability would also act as a comparison for future MB experiments. Spheroids were cultured off-chip, and subsequently loaded and trapped across 38 chips ($n = 185$ spheroids). Trapped spheroids were exposed to DOX for 8 h. DOX was then removed from the device, then fresh media added and replaced every 24 h. 48 h after exposure, NucRed Dead cell stain was added to the inlet reservoir then washed away after 30 min. Spheroids were imaged using confocal fluorescence microscopy to observe DOX accumulation and cell death. Fig. 3a shows spheroids trapped on-chip 48 h after being exposed to different concentrations of DOX (0 (control), 1, 5 and 7.5 μM). The left column shows the brightfield images of spheroids, with the middle column showing the corresponding fluorescence emission from DOX and the right column the emission from the dead stain.

Spheroids exposed to 1 μM DOX showed no observable reduction in spheroid integrity, with relatively low levels of DOX observed throughout the spheroid and few dead cells around the spheroid periphery. A 5 μM DOX exposure resulted in significant spheroid degradation. The outer layers of the spheroid appear to break down and emission from the dead stain confirms mass cell death in these layers. High levels of DOX emission were observed in the spheroid core, which still appeared intact and alive. Exposure to 7.5 μM DOX caused further

degradation of the outer layers. The mass cell death resulted in the loss of spheroid integrity, which gave rise to the outer layers of the spheroid being washed away under flow as the spheroid was unable to maintain its structure. The spheroid core remaining in the trap also showed dead cell fluorescence, suggesting the spheroid was minimally viable. Cells broken away from degraded spheroids could be observed to collect in the base of the outlet reservoir. The backflow used to collect spheroids also collected these fragments, so that analysis using ATP included all cells cultured in the device, alive and dead.

Spheroids were retrieved off chip by first adding media to the outlet reservoir to reverse the flow direction. A pipette was then attached to the inlet and very carefully withdrawn, pulling the spheroids from their traps. This could be achieved with low flow velocities due to the minimal adhesion of spheroids to PDMS. Spheroids were then analysed using CellTiter-Glo 3D cell viability assay. This assay, specifically designed for 3D spheroid cultures, lyses all of the cells, releasing ATP – a direct indicator of cellular viability. The ATP is then converted to a luciferase product which is detected as luminescence using a plate reader. The luminescence of the DOX-treated spheroids was then expressed as a percentage with respect to control spheroids that had simply been allowed to grow untreated for 48 h. Fig. 3b shows percentage spheroid viability for each DOX exposure with a dose response curve fitted to determine the IC₅₀ value. ATP assay results showed that 1 μM DOX had minimal effects on spheroid viability $91 \pm 8\%$, 5 μM DOX had a greater effect on viability $45 \pm 9\%$, whilst 7.5 μM DOX reduced spheroid viability substantially $27 \pm 9\%$. A higher dose of 10 μM DOX had only a slight increased effect on spheroid viability $20 \pm 2\%$ compared to 7.5 μM. The remaining cells were likely to be quiescent cells which show resistance to many therapies due to minimal uptake of drugs as a result of low metabolic activity [53]. The dose-response curve revealed an IC₅₀ value of 4 ± 0.1 μM. The IC₅₀ indicated that a concentration of 3 μM would be ideal for free DOX and MB co-delivery experiments. This dosage resulted in a small reduction in spheroid viability $75 \pm 4\%$ when administered as free drug alone, allowing for further reductions in viability to be demonstrated by the same DOX concentration, but including MBs. Overall, the agreement between imaging observations and ATP assay results gave confidence in the system's ability to produce reliable, consistent results.

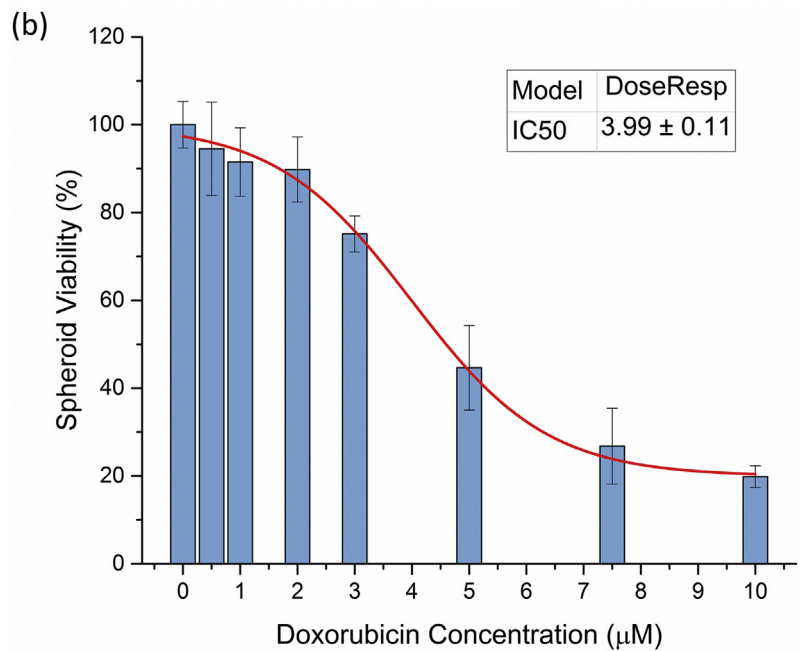
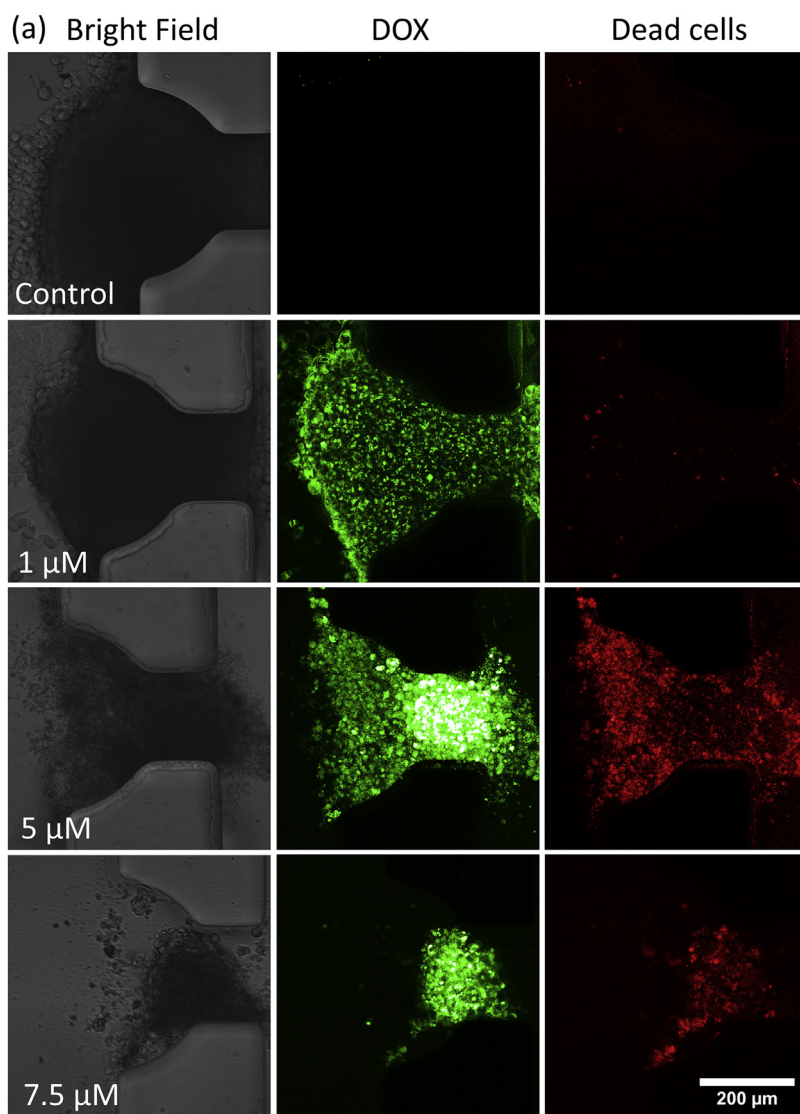


Fig. 3. (a) Bright field, doxorubicin (DOX) and dead cell (NucRed Dead) fluorescent emission from spheroids 48 h post exposure to 0 (control), 1, 5 and 7.5 μM DOX. (b) Spheroid viability with increasing concentrations of DOX, measured 48 h post exposure with CellTiter-Glo 3D cell viability assay ($n = 146$).

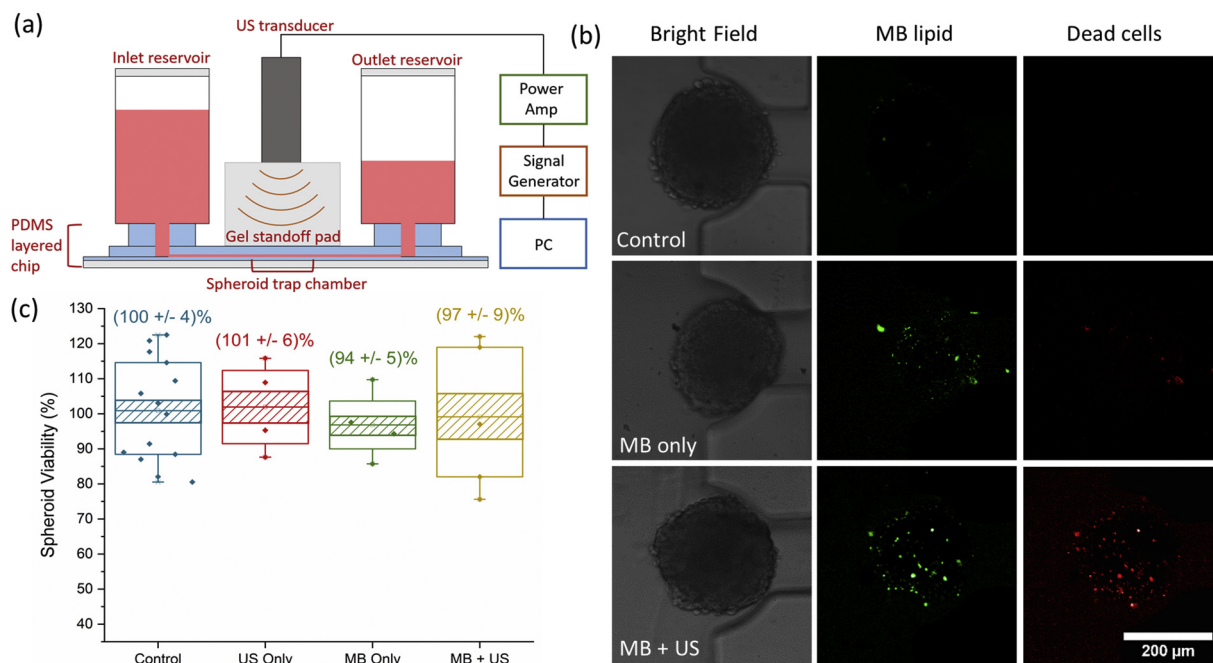


Fig. 4. a) Diagram of ultrasound setup with microfluidic chip and transducer. b) Bright field, Atto 488 lipid and dead cell (NucRed Dead) fluorescent emission from spheroids 8 h post exposure to MBs with and without US. c) A boxplot of spheroid viability with US, MB and MB + US exposures. Each data point represents a single chip. Box plots show range (whiskers), interquartile range (outer box), 95% confidence interval (hashed box) and mean (line). Annotated values show (mean \pm S.E).

3.3. Ultrasound and microbubble spheroid exposure

To determine the effect of co-delivering DOX with MBs, it was first necessary to observe the effect of the US trigger (+ US) alone, MBs (without US) and MBs + US exposures on spheroid viability. Fig. 4a shows the experimental setup used to expose the spheroid chamber to US. MB destruction in the device was tested under stopped flow conditions. Observation of MB concentrations across the chamber before and after US insonation found that 99.96 % of MBs were destroyed by the US pulse (Supplementary Fig. S6).

Spheroids were loaded into the chamber and exposed to the US trigger only ($n = 24$), MB only ($n = 12$) and MB + US ($n = 26$). 30 μ L of MBs (10^8 bubbles/mL) were loaded on chip then media was added to initiate flow. Supplementary Video 1 shows MBs in the trap array, flowing over and around the spheroids. MB + US chips were then exposed to the US trigger in order to destroy the MBs. In order to better observe the interaction between MBs (+US) and tumour spheroids, fluorescent Atto488 (0.2 mol%) lipids were incorporated into the lipid shell of the MBs during production. Observation of lipid deposition and associated cell death would indicate that effective MB-induced sonoporation was occurring. An increase in lipid transfer from MBs after destruction would also suggest that this effect would facilitate uptake of DOX-LS conjugated to MBs. Spheroids exposed to MB only and MB + US were imaged 8 h after exposure, with NucRed dead stain again being used to observe any cell death.

Fig. 4b shows images taken of control, MB only and MB + US spheroids trapped on-chip, 8 h after exposure. Brightfield images (left column) show no observable spheroid degradation in any of the experimental conditions. Lipid deposition (central column, Atto 488 fluorescence) shows negligible signal in control spheroids, as expected. Spheroids exposed to MB only showed small amounts of fluorescent lipid scattered across the surface whereas, spheroids exposed to MB + US showed increased amounts of fluorescent lipid deposition. Together these images indicate that fluorescent lipids from MBs are passively exchanged with spheroids as MBs flow across the surface. In contrast, destruction of MBs using US results in greater amounts of lipid exchange as lipids are sonoprinted onto the spheroid surface.

Comparison of dead cell detection (right column, NucRed fluorescence) showed minimal cell death occurred in MB alone treatment. Whereas, when the MBs had been destroyed, multiple dead cells were visible on the surface of the spheroid which were directly associated with fluorescent lipid locations. The correlation of lipids and cell death indicated that MB destruction with US resulted in irreversible sonoporation, in which cell death occurs as a result of pore formation in cell membranes.

Fig. 4c shows the ATP assay results for each of the experimental conditions. Comparison of spheroid viabilities from US only ($101 \pm 6\%$), MB only ($94 \pm 5\%$) and MB + US ($97 \pm 9\%$) exposures showed no statistically significant difference compared to control values when subjected to a Mann-Whitney (MW) non-parametric U test. To better evaluate the data obtained in each exposure, a 95% confidence interval test was performed on each data set. This value describes the range around the mean in which there is a 95% certainty it contains the true mean. This was determined to be $\pm 3.2\%$, $\pm 4.5\%$, $\pm 2.7\%$ and $\pm 6.6\%$ for control, US only, MB only and MB + US exposures. The overlap of confidence intervals with the control interval gave further evidence that these exposures were not having a significant effect on spheroid viability. Overall, the spheroid viability results confirmed that these control exposures to MB and MB + US had no adverse effects on the spheroid's structural integrity or viability. Lower viabilities were observed across two sets of spheroids exposed to MB + US. This could be attributed to the cell death cause by MB destruction which is indicative of irreversible sonoporation where pores fail to reseal after insonation [54]. Hu et al. observed this effect alongside many other partial membrane perforations that eventually resealed [55]. That study used a 1:1 MB to cell ratio, here the ratio of nearby MBs to outer layer spheroid cells only is estimated to be approximately 1.5:1, suggesting similar numbers MB sonoporation events will be occurring. However this estimate cannot account for the effects of flow on local MB concentrations or any potential MB accumulation. The NucRed dead cell stain used throughout this series of experiments is comparable to propidium iodide (PI) which is often used to study the production of pores from MB sonoporation. Both compounds only become fluorescent when entering a perforated cell membrane, allowing for the observation of compromised cell membranes. Considerable

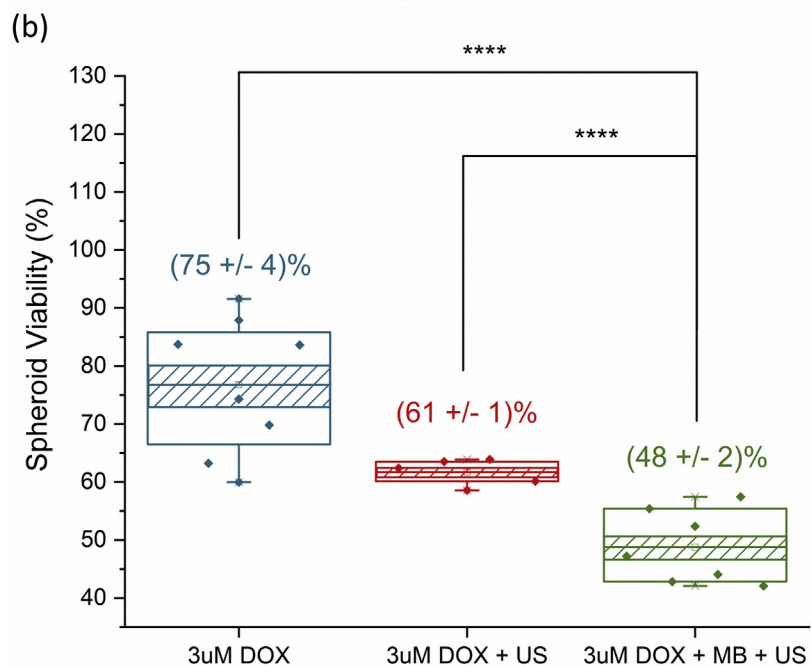
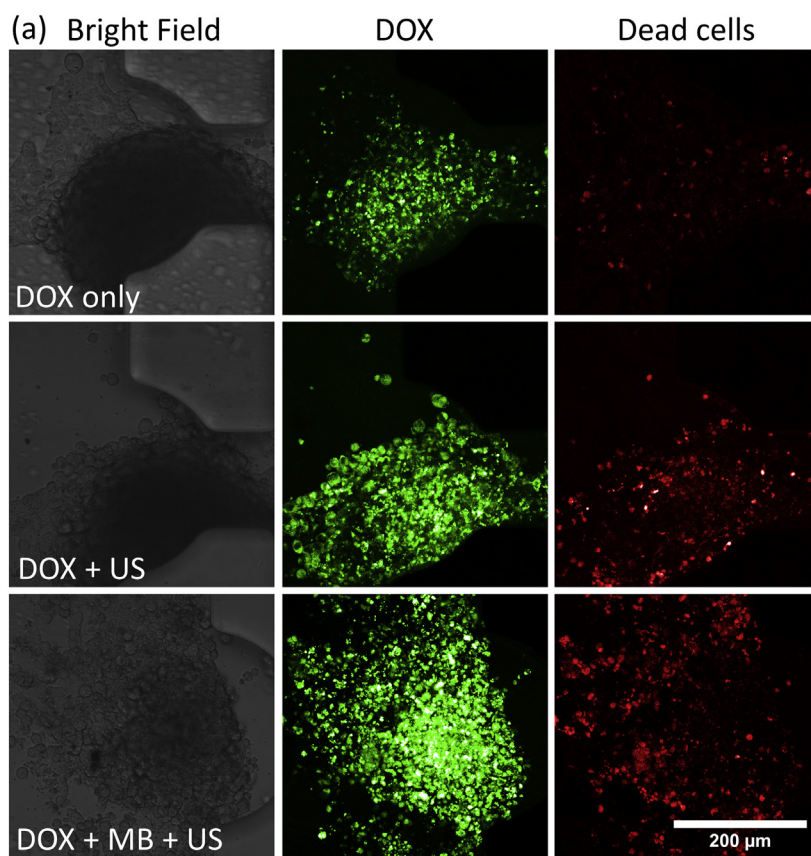


Fig. 5. (a) Bright field, DOX and dead cell (NucRed Dead) fluorescent emission from spheroids 48 h post exposure to 3 μM DOX only, with US and with MB + US. (b) Spheroid viability for spheroids 48 h post exposure to 3 μM DOX free drug alone ($n = 39$), with US ($n = 26$) and with MB + US ($n = 31$). Each data point represents a single chip.

numbers of dead cells could be observed in spheroids exposed to MB + US, however this appeared to have minimal effect on the overall spheroid viability measured 48 h later.

3.4. Co-delivery of free DOX with MBs + US

Next, the effectiveness of US triggered MBs as drug delivery enhancers was investigated by co-delivering 3 μM DOX with MBs to spheroids. The experiment was performed using the same setup and

time points as in previous sections, to allow for direct comparison between results. Along with the complete therapeutic combination of DOX + MB + US, a control DOX + US (without MBs) was included for comparison. Fig. 5a shows brightfield, DOX emission and NucRed emission cell images taken of spheroids 48 h post-exposure to each of the conditions. A trend in decreasing spheroid structural integrity and core density with DOX only, DOX + US then DOX + MB + US can be observed in brightfield images. Similar observations were made with increasing free drug concentrations and is indicative of increased drug penetration and decreased spheroid integrity. Decreased core density was also accompanied by evidence of cells shedding from the outer layers of the spheroid, an effect which only occurred in spheroids subjected to higher concentrations of DOX in previous experiments. Fluorescent DOX imaging shows a clear increase in fluorescence intensity from DOX only treatment to the complete exposure condition. This suggests that DOX + US and DOX + MB + US exposures allow for increased DOX accumulation into spheroids. Fluorescence from dead cells was only observed around the periphery of spheroids exposed to DOX only. However, dead cells were found much further into the centre of the spheroid when DOX was delivered alongside MB + US, suggesting the destruction of the MBs in close proximity increased drug penetration into the spheroids.

Spheroids were once again retrieved using backflow and the ATP assay used to quantify spheroid viability. Fig. 5b shows the boxplot of spheroid viability for each therapeutic exposure. Results show that the combination of 3 μM DOX + US (without MB) reduced spheroid viability to $61 \pm 1\%$, and 3 μM DOX + US + MB reduced viability to $48 \pm 2\%$. These values were both significantly lower than that of free 3 μM DOX $75 \pm 4\%$. The p values in each case were found to be < 0.0001 (****), illustrating the highly significant statistical difference between the groups.

The free DOX dose response curve indicates that a DOX concentration of approximately 4.8 μM would be required to reduce spheroid viability to 45%. This indicated an increase in DOX efficacy at the lower concentration of 3 μM of approximately 60% when co-delivered with MB + US. Spheroids exposed to free 5 μM showed a similar viability $45 \pm 9\%$ to the 3 μM DOX + MB + US along with comparable amounts of drug accumulation and cell death (Fig. 3(a) and 5(a)), suggesting that the presence of MBs and US allowed for lower doses of DOX to be delivered for an equivalent therapeutic effect. It is evident that the sonoporation caused by MB destruction increased drug penetration and accumulation and overall effectiveness of the DOX. These observations are in agreement with previous studies into the effects of sonoporation on the delivery of drugs to tumours [56,57]. Escoffre et al. show that co-delivery of DOX and MBs enhanced both early and late stage DOX-induced cell apoptosis, leading to a similar increase in DOX efficacy as observed in this study [58]. However, this study was conducted on static glioblastoma and breast cell monolayers and relied on live/dead cell counting assays for viability results. Thus limiting the validity of a comparison between our studies. It was also observed in these experiments that DOX efficacy was improved with the use of US alone, giving an average spheroid viability of $61 \pm 1\%$. In the previous control, US alone was observed to have no significant effect on spheroid viability, indicating that there may be an interaction between DOX and US that increases drug efficacy. One explanation for this effect is US-induced acoustic streaming exerting shear stress on cell membranes and increasing permeability [59,60]. Similar synergistic effects of DOX + US co-delivery have previously been observed and become more significant with longer and more intense US exposures [57,61–63].

3.5. Co-delivery of drug loaded MBs with US trigger

The previous results showed the efficacy of free DOX + MB + US when administered to CRC spheroids. However, in a clinical setting, the use of free DOX presents many limitations due to its cardiopathic

side effects. Encapsulation of DOX inside LS provided a solution to this issue - with liposomal DOX being observed to have an improved toxicity profile and reduced cardiac effects compared to its free counterpart. Conjugation of DOX LS to MBs offers a method by which DOX can be delivered locally to tumours. Insonation of these drug-loaded MBs (DLMBs) at the tumour site would allow for release and uptake of DOX-LS exclusively in surrounding tumour tissues. The following experiments investigated the effects of DOX-LS only, DOX-LS co-delivered with MBs and US (DOX-LS + MB + US) and finally, DOX-LS conjugated to the lipid shell of the MBs, delivered with US (DLMBs + US). This allowed for the effects of DOX-LS, with no MBs, unconjugated MBs and conjugated MBs on spheroids to be observed. In addition to this, the effect of multiple US exposures with DLMBs was investigated. The volume of the spheroid chamber is $\sim 6\ \mu\text{L}$, meaning the entire 30 μL DLMB solution could fill the chamber 5 times. Separate DLMB-spheroid chips were therefore exposed to 1, 3 and 5 US exposures with 60s given between each exposure to allow the chamber to refill with DLMBs. This was to define whether multiple DLMB destructions increased drug delivery to spheroids.

DLMBs were produced as described in the methods. In order to investigate the effect of DOX-LS and DLMBs compared to free DOX of previous experiments, the concentration of DOX-LS was adjusted to deliver an equivalent DOX concentration of 3 μM . DLMBs were produced so that the same number of MBs and total DOX dose was contained within the 30 μL solution administered to each chip. This was followed by the same volume of medium used in free DOX experiments to keep the total volume consistent. The same exposure regime and analysis was performed as in previous sections.

Fig. 6a shows bright field, DOX emission and NucRed dead stain fluorescence emission from spheroids exposed to DOX-LS, DOX-LS + MB + US and DLMB + US (x3). Comparison of DOX accumulation in spheroids exposed to DOX-LS and DOX-LS + MB + US shows little difference in drug penetration or DOX accumulation. A similar number of dead cells were also observed across each set of spheroids. This suggests that the co-delivery of DOX-LS + MB + US does not facilitate the delivery of DOX-LS into tumour spheroids. The pores created in the cell membrane from MB sonoporation must not allow for substantial transfer of DOX-LS into the cell. Spheroids exposed to DLMB + US (x3) showed increased DOX accumulation and dead cell detection in the outer layers of the spheroids when compared conditions in which DOX-LS were not attached to the MB surface. However, there was no observable trend in the amount of DOX accumulated or number of dead cells with the number of DLMB + US exposures (Supplementary Fig. S7). This indicated that the maximum therapeutic effect is achieved after only one US exposure.

Fig. 6b shows the boxplot of spheroid viability after DOX-LS, DOX-LS + MB + US and DLMB US (x1, 3 and 5) exposures. Analysis of spheroids after DOX-LS and DOX-LS + MB + US exposures found mean viability values of $74 \pm 3\%$ and $76 \pm 3\%$ respectively. No statistical significance was found between the datasets, further substantiating that increased DOX-LS accumulation does not occur when DOX-LS are co-delivered rather than conjugated to MBs. Spheroid viability showed no difference with repeated DLMB + US exposures - $59 \pm 5\%$, $61 \pm 6\%$ and $65 \pm 4\%$ for DLMB US x1, x3, and x5 respectively. This was in agreement with imaging observations which also showed no substantial differences in cell death or drug accumulation. Comparison between spheroid viabilities from DOX-LS and DLMB exposures found statistically significant differences with every number of US exposures, again agreeing with imaging observations.

Exposure of spheroids to DOX-LS, with and without unconjugated MBs, was found to have an equivalent effect on spheroid viability when compared to an equal dose of free DOX. This largely disagrees with previous studies which often show free DOX having a greater effect over DOX-LS. The apparent increase in liposomal DOX efficacy observed in this study could be attributed to increased mass transport of DOX-LS into the outer layers of spheroids. Increased mass transport due to the

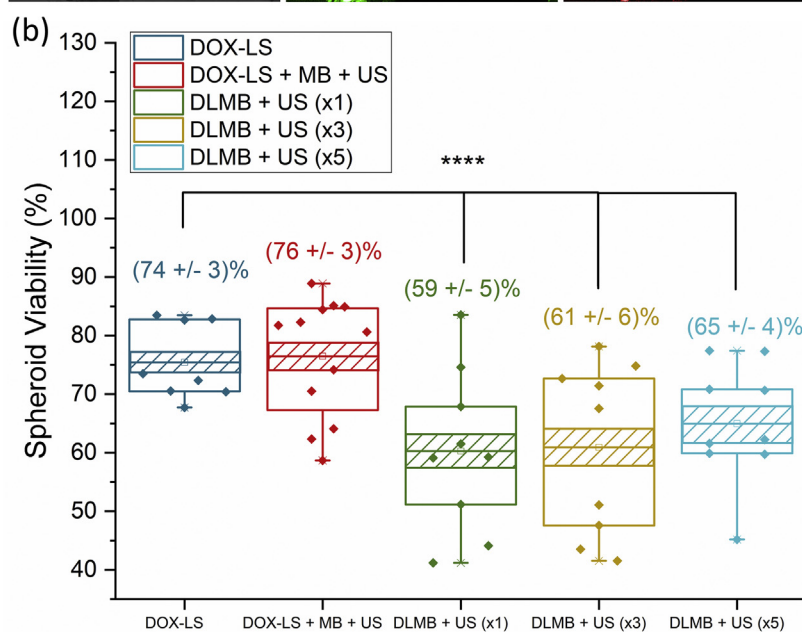
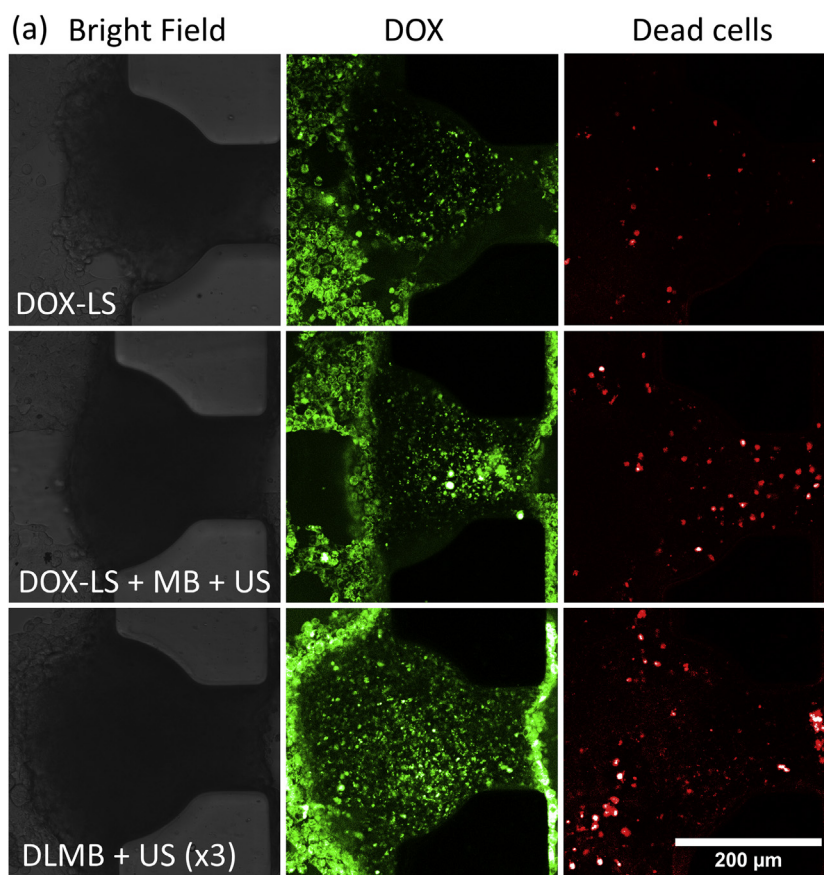


Fig. 6. (a) Bright field, DOX and dead cell (NucRed Dead) fluorescent emission from spheroids 48 h post-exposure to Free LS, LS + MB (free) and DLMB US x3. (b) Spheroid viability for spheroids 48 h post exposure to Free LS ($n = 38$), LS + MB (free) ($n = 66$), DLMB x1 ($n = 73$), x3 ($n = 70$) and x5 ($n = 71$). Each data point represents a single chip.

shear stress induced from fluid flow would demonstrate that the presence of fluid flow is a very important parameter in drug studies. Research from Kang et al. found that the uptake of polystyrene nanospheres was increased on average 50% for a range of tumour cell lines, due to biomimetic rates of shear stress [64,65]. Shear stress has also been found to increase the effectiveness of liposomal DOX compared to

static delivery, however this study again demonstrated that free DOX reduced cell viability more than of liposomal DOX [66]. Another potential reason for the increase in DOX-LS efficacy is the method by which the drug is delivered on-chip. A total dose of DOX-LS equivalent to the 2 mL, 3 μM free DOX dose was initially loaded on-chip in a 30 μL volume, then followed by 2 mL of media. The initial local DOX-LS

concentration will therefore be considerably higher and may have allowed for increased instantaneous accumulation, further facilitated by the inertial cavitation of MBs.

DOX-LS did not show any increased efficacy when delivered alongside free MBs + US (Fig. 6b). Similar amounts of fluorescent DOX emission from each set of spheroids suggests that the sonoporation induced by MB bursting does not facilitate the effective delivery of unconjugated DOX-LS to the outer layers of the spheroid. In contrast to the co-delivery of DOX-LS and MBs, DLMBs were found to be more effective in decreasing spheroids viability. Similar results were observed by Roovers et al. which, also found a lack of increased DOX-LS efficacy when no conjugated to MBs + US [36]. Assay results show that, on average, DLMB's reduced spheroid viability to $62 \pm 3\%$, a decrease of approximately 15% from DOX-LS and DOX-LS + MB + US exposures. Spheroid viability across each DLMB exposure was found to vary considerably suggesting that there is either varying amounts of DOX-LS being delivered to the spheroids or, varying amounts of release occurring from the DOX-LS. Allowing a longer period of time between drug exposure and analysis of viability may reduce the spread in data as more complete DOX release from DOX-LS occurs. However, this would only be the case if similar numbers of DOX-LS were being delivered to each spheroid. This could also allow for the effects of MB-enhanced drug delivery to be better observed, as the effects of increased LS accumulation become more significant with time. Interestingly, the number of US exposures did not appear to have an effect on the amount of DOX delivered to spheroids. It is suggested that the outer layers of cells in the spheroid become saturated with DOX-LS after the first US exposure, rendering any further exposures ineffective as more DOX-LS are delivered to cells already containing cytotoxic numbers of DOX-LS. Perhaps a more effective treatment regime could use repeat exposures with longer time intervals. This could allow time for the initial DOX-LS exposure to take effect and cause outer layer cell death. Subsequent exposures would then target the remaining healthy cells revealed as outer layer cells die.

Confocal imaging of DOX accumulation throughout spheroids exposed to DLMB shows DOX-LS were mainly found localised to the outer cell layers. What was most interesting about this observation, is the fact that the cells in which DOX was observed are not present in the spheroid at the time of treatment. These outer layer cells imaged 48 h after treatment were observed to grow within the first 24 h and were not present in the outer layers of the spheroid at the time of treatment. It is suggested that the initial slow release kinetics of DOX from the liposomes allows for cells to continue to divide even after the initial DLMB treatment, due to the early-stage non-toxic concentrations of DOX. As more DOX is released from LS, concentrations become significant enough to cause cytotoxic effects and decrease spheroid viability. The release of DOX from Doxil and similar DOX-LS under physiological conditions has previously been reported to be very slow, showing only 5% release over 24 h [67]. Seynhaeve et al. studied the intracellular release of DOX from Doxil LS, comparing results with free DOX treatments [68]. Measuring the amount of DOX within cells 24 h after treatment found significantly lower amounts from cells exposed to Doxil, indicating minimal DOX release across this time. Similar observations were also made by Roovers et al. in a recent MB spheroid paper, in which DOX-LS were found to release little DOX 72 h after MB destruction [36].

Contrary to these observations, spheroids exposed to DOX-LS throughout this study were growth inhibited by a substantial amount in any exposure. These viabilities, along with imaging observations, suggest that significant amounts of DOX was being released from LS throughout the 48 h period. A potential mechanism for this release could be presence of ammonia at the tumour spheroid site. Ammonia is produced by tumour cells by glutaminolysis, the metabolic process which tumour cells often favour over the normal glycolytic pathway in order to meet cell energy requirements [69]. A recent study investigated drug release from Doxil with ammonia, finding that drug

release is increased up to 80% across 48 h in the presence 50 mM ammonium sulphate [70]. This process of release is similar to that of the DOX-LS loading process, where the uncharged DOX diffuses across the liposome membrane and then becomes deprotonated, preventing it from passing back through the bilayer [71]. A further driver of this glutaminolysis release mechanism may be the hypoxic conditions created at the centre of tumour spheroids. The enzyme responsible for the production of glutamate and ammonia from glutamine, glutaminase 1 (GSL1) has been observed to be stimulated by the production of hypoxic inducible factor 1 (HIF1) in colorectal cancers. HIF1 is a potent inducer of cancer cell proliferation, invasion and metastasis, all of which were found to be dependent on the upregulation of GSL1 and subsequent glutaminolysis [69]. The lack of hypoxic conditions in the relatively small, 100 μm spheroids used throughout Roovers et al. (2019) MB study compared to the hypoxic conditions created at the centre of $\geq 300 \mu\text{m}$ spheroids throughout this study, may be a factor affecting the lack of drug release observed in their study. However, direct observation of GSL1/HIF1 involvement in DOX-LS release would be required to confirm this connection.

4. Conclusions

This study presented a new microfluidic device allowing for the trapping, culture and MB-therapeutic testing of tumour spheroid co-cultures under physiological flow conditions. The self-contained system design allowed for simple multiplexing, enabling the high throughput screening of multiple therapeutic conditions in parallel. The microfluidic trap design allowed for straightforward spheroid retrieval and subsequent quantitative analysis of spheroid viability. This was supplemented with confocal imaging, which enabled spheroid degradation, drug accumulation and cell death to be observed. The use of microfluidics to create *in vivo*-like rates of flow and shear stress further enhanced the physiological relevance of the 3D culture system. Indeed, several results observed throughout this paper could be attributed to the effects of flow-induced shear stress, and may provide further insight into the mechanism of these therapeutics *in vivo*.

Overall, the co-delivery of MBs + US with DOX has been shown to increase drug efficacy in both free and liposomal formulations. DLMBs have been shown offer a promising method of delivering drugs to tumours, offering both increased efficacy and localised delivery in comparison to DOX-LS alone. It is evident that bursting of DLMB facilitates the uptake of DOX-LS into the tumour tissue, however this process does not appear result in the release of DOX from DOX-LS. This is advantageous in minimising the systemic dose of DOX whilst also ensuring maximum localised DOX-LS delivery. The lack of associated vasculature within the spheroids limits the ability of this study to predict the extent of this effect *in vivo*, and the recently developed vasculature on-chip models may present a system where this could be further investigated [72–74]. It known that the endothelium will present an additional barrier that must be overcome to effectively deliver drugs to the tumour. However, endothelial cells have been shown to be equally as susceptible to the effects of MB induced sonoporation, suggesting that a similar increase in drug efficacy may be observed as in this study [75,76].

Supplementary data to this article can be found online at <https://doi.org/10.1016/j.jconrel.2020.06.011>.

Declaration of Competing Interest

There are no conflicts of interest to declare.

Acknowledgements

The authors would like to thank Dr. Julia Gala de Pablo for the assistance with the trap design framework calculations. We

acknowledge the following funders: Medical Research Council (MR/M009084/1) and Engineering and Physical Sciences Research Council (EP/P023266/1) and (EP/S001069/1). Kevin D'Silva for the provision of a PhD scholarship to Mr. D. Batchelor. S.D.E. is supported by the National Institute for Health Research infrastructure at Leeds. The views expressed are those of the author(s) and not necessarily those of the National Health Service, the National Institute for Health Research, or the Department of Health. The authors would also like to thank Dr. Mark D. Tarn for comments on the manuscript. The data used in these figures is available at <https://doi.org/10.5518/777>.

References

- J.W. Haycock, *Methods Mol. Biol.* 695 (2011) 1–15, <https://doi.org/10.1007/978-1-60761-984-0>.
- S. Sant, P.A. Johnston, *Drug Discov. Today Technol.* 23 (2017) 27–36, <https://doi.org/10.1016/j.ddtec.2017.03.002>.
- B.K. Jong, *Semin. Cancer Biol.* 15 (2005) 365–377.
- C.R. Thoma, M. Zimmermann, I. Agarkova, J.M. Kelm, W. Krek, *Adv. Drug Deliv. Rev.* 69–70 (2014) 29–41, <https://doi.org/10.1016/j.addr.2014.03.001>.
- E. Fennema, N. Rivron, J. Rouwkema, C. van Blitterswijk, J. De Boer, *Trends Biotechnol.* 31 (2013) 108–115, <https://doi.org/10.1016/j.tibtech.2012.12.003>.
- O.I. Hoffmann, C. Ilmberger, S. Magosch, M. Joka, K.W. Jauch, B. Mayer, *J. Biotechnol.* 205 (2015) 14–23, <https://doi.org/10.1016/j.jbiotec.2015.02.029>.
- M. Vinci, S. Gowan, F. Boxall, L. Patterson, M. Zimmermann, W. Court, C. Lomas, M. Mendiola, D. Hardisson, S.A. Eccles, *BMC Biol.* 10 (2012) 29.
- D. Yip, C.H. Cho, *Biochem. Biophys. Res. Commun.* 433 (2013) 327–332, <https://doi.org/10.1016/j.bbrc.2013.03.008>.
- N.A. Bhowmick, E.G. Neilson, H.L. Moses, *Nature* 432 (2004) 332–337 <http://www.ncbi.nlm.nih.gov/pubmed/15549095> <http://www.pubmedcentral.nih.gov/articlerender.fcgi?artid=PMC3050735>.
- J. Webber, R. Steadman, M.D. Mason, Z. Tabi, A. Clayton, *Cancer Res.* 70 (2010) 9621–9630.
- V.G. Peddareddigari, D. Wang, R.N. Dubois, *Cancer Microenviron.* 3 (2010) 149–166.
- A. Calon, E. Espinet, S. Palomo-Ponce, D.V.F. Tauriello, M. Iglesias, M.V. Céspedes, M. Sevillano, C. Nadal, P. Jung, X.H.-F. Zhang, D. Byrom, A. Riera, D. Rossell, R. Mangues, J. Massague, E. Sancho, E. Battle, *Cancer Cell* 22 (2012) 571–584.
- F. Lotti, A.M. Jarrar, R.K. Pai, M. Hitomi, J. Lathia, A. Mace, G.A. Gantt, K. Sukhdeo, J. DeVecchio, A. Vasanthi, P. Leahy, A.B. Hjelmeland, M.F. Kalady, J.N. Rich, *J. Exp. Med.* 210 (2013) 2851–2872.
- N. Mukaida, S. Sasaki, *World J. Gastroenterol.* 22 (2016) 5301–5316.
- A.C. Newman, M.N. Nakatsu, W. Chou, P.D. Gershon, C.C.W. Hughes, *Mol. Biol. Cell* 22 (2011) 3791–3800, <https://doi.org/10.1091/mbc.E11-05-0393>.
- C.G. Alexis Desmoulière, G.G. Alexis Desmoulière, *517 (2004) 509–517* <http://www.ijdb.ehu.es/web/paper.php?doi=10.1387/ijdb.041802ad>.
- Y. Koshida, M. Kuranami, M. Watanabe, *J. Surg. Res.* 134 (2006) 270–277.
- T. Tsujino, I. Seshimo, H. Yamamoto, Y.N. Chew, K. Ezumi, I. Takemasa, M. Ikeda, M. Sekimoto, N. Matsuura, M. Monden, *Clin. Cancer Res.* 13 (2007) 2082–2090.
- M. Herrera, A. Herrera, G. Domínguez, J. Silva, V. García, J.M. García, I. Gómez, B. Soldevilla, C. Muñoz, M. Provencio, Y. Campos-Martin, A. García de Herreros, I. Casal, F. Bonilla, C. Peña, *Cancer Sci.* 104 (2013) 437–444.
- O. De Wever, P. Demetter, M. Mareel, M. Bracke, *Int. J. Cancer* 123 (2008) 2229–2238.
- P.J. Morin, *Drug Resist. Updat.* 6 (2003) 169–172.
- A.I. Minchinton, I.F. Tannock, *Nat. Rev. Cancer* 6 (2006) 583–592.
- T. Sethi Tevior, R.C. Rintoul, S.M. Moore, A.C. MacKinnon, D. Salter, C. Choo, E.R. Chilvers, I. Dransfield, S.C. Donnelly, R. Strieter, C. Haslett, *Nat. Med.* 5 (1999) 662–668 <http://www.ncbi.nlm.nih.gov/pubmed/10371505>.
- T. Boissenot, A. Bordat, E. Fattal, N. Tsapis, *J. Control. Release* 241 (2016) 144–163, <https://doi.org/10.1016/j.jconrel.2016.09.026>.
- M. Wang, Y. Zhang, C. Cai, J. Tu, X. Guo, D. Zhang, *Sci. Rep.* 8 (2018) 1–12, <https://doi.org/10.1038/s41598-018-22056-8>.
- I. De Cock, E. Zagato, K. Braeckmans, Y. Luan, N. de Jong, S.C. De Smedt, I. Lentacker, *J. Control. Release* 197 (2015) 20–28, <https://doi.org/10.1016/j.jconrel.2014.10.031>.
- H. Lee, J. Han, H. Shin, H. Han, K. Na, H. Kim, *J. Control. Release* 283 (2018) 190–199, <https://doi.org/10.1016/j.jconrel.2018.06.008>.
- I. Lentacker, B. Geers, J. Demeester, S.C. De Smedt, N.N. Sanders, *Mol. Ther.* 18 (2010) 101–108, <https://doi.org/10.1038/mt.2009.160>.
- K. Kooiman, H.J. Vos, M. Versluis, N. De Jong, *Adv. Drug Deliv. Rev.* 72 (2014) 28–48, <https://doi.org/10.1016/j.addr.2014.03.003>.
- T.A. Wynn, D. Ph, L. Barron, *Liver* 30 (2011) 245–257.
- J. McLaughlan, N. Ingram, P.R. Smith, S. Harput, P.L. Coletta, S. Evans, S. Freear, *IEEE Trans. Ultrason. Ferroelectr. Freq. Control* 60 (2013) 2511–2520.
- R. Leenhardt, M. Camus, J.L. Mestas, M. Jeljeli, E. Abou Ali, S. Chouzenoux, B. Bordacahar, C. Nicco, F. Bateau, C. Lafon, *F. Prat, Sci. Rep.* 9 (2019) 1–9.
- A. Yudina, M. Lepetit-Coiffé, C.T.W. Moonen, *Mol. Imaging Biol.* 13 (2011) 239–249.
- S.W. Fong, E. Klaseboer, B.C. Khoo, *J. Acoust. Soc. Am.* 123 (2008) 3223.
- E.A. Brujan, *J. Phys. D. Appl. Phys.* 50 (2017).
- S. Roovers, J. Deprez, D. Priwitaningrum, G. Lajoinie, N. Rivron, H. Declercq, O. De Wever, E. Stride, S. Le Gac, M. Versluis, J. Prakash, S.C. De Smedt, I. Lentacker, *J. Control. Release* (2019) 112062, <https://doi.org/10.1016/j.jphotochem.2019.112062>.
- K. Logan, F. Foglietta, H. Nesbitt, Y. Sheng, T. McKaig, S. Kamila, J. Gao, N. Nomikou, B. Callan, A.P. McHale, J.F. Callan, *Eur. J. Pharm. Biopharm.* 139 (2019) 224–231, <https://doi.org/10.1016/j.ejpb.2019.04.003>.
- A.Y. Hsiao, Y. Suke Torisawa, Y.C. Tung, S. Sud, R.S. Taichman, K.J. Pienta, S. Takayama, *Biomaterials* 30 (2009) 3020–3027, <https://doi.org/10.1016/j.biomaterials.2009.02.047>.
- J. Ruppen, L. Cortes-Dericks, E. Marconi, G. Karoubi, R.A. Schmid, R. Peng, T.M. Marti, O.T. Guenat, *Lab Chip* 14 (2014) 1198–1205.
- C. Kim, S. Chung, Y.E. Kim, K.S. Lee, S.H. Lee, K.W. Oh, J.Y. Kang, *Lab. Chip* 11 (2011) 246–252.
- J.Y. Kim, D.A. Fluri, R. Marchan, K. Boonen, S. Mohanty, P. Singh, S. Hammad, B. Landuyt, J.G. Hengstler, J.M. Kelm, A. Hierlemann, O. Frey, *J. Biotechnol.* 205 (2015) 24–35, <https://doi.org/10.1016/j.jbiotec.2015.01.003>.
- P. Sabhachandani, V. Motwani, N. Cohen, S. Sarkar, V. Torchilin, T. Konry, *Lab Chip* 16 (2016) 497–505.
- M. Astolfi, B. Péant, M.A. Lateef, N. Rousset, J. Kendall-Dupont, E. Carmona, F. Monet, F. Saad, D. Provencher, A.M. Mes-Masson, T. Gervais, *Lab Chip* 16 (2016) 312–325.
- K.H. Elaine, N. Marieb, *Human Anatomy & Physiology*, (2013).
- C. Mack, *Fundamental Principles of Optical Lithography: The Science of Microfabrication*, Wiley, 2011.
- P. Kim, K.W. Kwon, M.C. Park, S.H. Lee, K.Y. Suh, S.M. Kim, *Biochip J.* 2 (2008) 1–11.
- W. Chen, C. Wong, E. Vosburgh, A.J. Levine, D.J. Foran, E.Y. Xu, *J. Vis. Exp.* (2014) 1–10 <http://www.jove.com/video/51639/high-throughput-image-analysis-tumor-spheroids-user-friendly-software>.
- S.A. Peyman, R.H. Abou-Saleh, J.R. McLaughlan, N. Ingram, B.R.G. Johnson, K. Critchley, S. Freear, J.A. Evans, A.F. Markham, P.L. Coletta, S.D. Evans, *Lab Chip* 12 (2012) 4544–4552.
- X. Xu, P. Sarder, Z. Li, A. Nehorai, *Biomicrofluidics* 7 (2013) 1–16.
- D. Di Carlo, L.Y. Wu, L.P. Lee, *Lab Chip* 6 (2006) 1445–1449.
- H. Bruus, *Theoretical Microfluidics*, Oxford University Press, 2008.
- L. Chau, M. Doran, J. Cooper-White, *Lab Chip* 9 (2009) 1897–1902.
- J.P. Freyer, *J. Cell. Physiol.* 176 (1998) 138–149.
- T. van Rooij, I. Skachkov, I. Beekers, K.R. Latwein, J.D. Voorneveld, T.J.A. Kokhuis, D. Bera, Y. Luan, A.F.W. van der Steen, N. de Jong, K. Kooiman, *J. Control. Release* 238 (2016) 197–211, <https://doi.org/10.1016/j.jconrel.2016.07.037>.
- Y. Hu, J.M.F. Wan, A.C.H. Yu, *Ultrasound Med. Biol.* 39 (2013) 2393–2405.
- P. Nittayacharn, H.X. Yuan, C. Hernandez, P. Bielecki, H. Zhou, A.A. Exner, *J. Pharm. Sci.* 108 (2019) 3091–3098, <https://doi.org/10.1016/j.xphs.2019.05.004>.
- T. Yoshida, T. Kondo, R. Ogawa, L.B. Feril, Q.L. Zhao, A. Watanabe, K. Tsukada, *Cancer Chemother. Pharmacol.* 61 (2008) 559–567.
- J.M. Escoffe, J. Piron, A. Novell, A. Bouakaz, *Mol. Pharm.* 8 (2011) 799–806.
- J. Wu, *Fluids* 3, (2018).
- T. Leong, M. Ashokkumar, S. Kentish, *Handbook of Ultrasonics and Sonochemistry*, (2016).
- S.I. Umemura, N. Yumita, Y. Okano, M. Kaneuchi, N. Magario, M. Ishizaki, K. Shimizu, Y. Sano, K. Umemura, R. Nishigaki, *Cancer Lett.* 121 (1997) 195–201.
- L. Liang, S. Xie, L. Jiang, H. Jin, S. Li, J. Liu, *Ultrasound Med. Biol.* 39 (2013) 146–160.
- R. Teranishi, T. Matsuda, E. Yuba, K. Kono, A. Harada, *Macromol. Biosci.* 19 (2019) 1–9.
- T. Kang, C. Park, B.J. Lee, *Arch. Pharm. Res.* 39 (2016) 1663–1670.
- T. Kang, T.T.T. Tran, C. Park, B.J. Lee, *J. Pharm. Investig.* 47 (2017) 133–139.
- L. Hosta-Rigau, B. Städler, *Mol. Pharm.* 10 (2013) 2707–2712.
- L.M. Russell, M. Hultz, P.C. Searson, *J. Control. Release* 269 (2018) 171–176, <https://doi.org/10.1016/j.jconrel.2017.11.007>.
- A.L.B. Seynhaeve, B.M. Dicheva, S. Hoving, G.A. Koning, T.L.M. Ten Hagen, *J. Control. Release* 172 (2013) 330–340, <https://doi.org/10.1016/j.jconrel.2013.08.034>.
- R.W. Moreadith, A.L. Lehninger, *J. Biol. Chem.* 259 (1984) 6215–6221.
- L. Silverman, Y. Barenholz, *Nanomedicine nanotechnology, Biol. Med.* 11 (2015) 1841–1850, <https://doi.org/10.1016/j.nano.2015.06.007>.
- A. Fritze, F. Hens, A. Kimpfler, R. Schubert, R. Peschka-Süss, *Biochim. Biophys. Acta Biomembr.* 1758 (2006) 1633–1640.
- X. Wang, D.T.T. Phan, A. Sobrino, S.C. George, C.C.W. Hughes, A.P. Lee, *Lab Chip* 16 (2016) 282–290 <http://xlink.rsc.org/?DOI=C5LC01050K>.
- Y. Nashimoto, T. Hayashi, I. Kunita, A. Nakamura, Y.S. Torisawa, M. Nakayama, H. Takigawa-Imamura, H. Kotera, K. Nishiyama, T. Miura, R. Yokokawa, *Integr. Biol. (United Kingdom)* 9 (2017) 506–518, <https://doi.org/10.1039/C7IB00024C>.
- A. Sobrino, D.T.T. Phan, R. Datta, X. Wang, S.J. Hachey, M. Romero-López, E. Gratton, A.P. Lee, S.C. George, C.C.W. Hughes, *Sci. Rep.* 6 (2016) 1–11, <https://doi.org/10.1038/srep31589>.
- G. Silvani, S. Scognamiglio, D. Caprini, L. Marino, M. Chinappi, G. Sinibaldi, G. Peruzzi, M.F. Kiani, C.M. Casciola, *Small* 15 (2019) 1–11.
- K. Kooiman, M. Foppen-Harteveld, A.F.W.V. Der Steen, N. De Jong, *J. Control. Release* 154 (2011) 35–41, <https://doi.org/10.1016/j.jconrel.2011.04.008>.